

---

# PHOTOACOUSTIC ITERATIVE OPTIMIZATION ALGORITHM WITH SHAPE PRIOR REGULARIZATION

---

**Zhang Yu**

Department of Biomedical Engineering  
College of Future Technology  
Peking University  
zyuaiyi1\_stu.pku.edu.cn

**Li Shuang**

Department of Biomedical Engineering  
College of Future Technology  
Peking University  
jaeger\_ls@stu.pku.edu.cn

**Wang Yibing**

Department of Biomedical Engineering  
College of Future Technology  
Peking University  
ddffwyb@pku.edu.cn

**Sun Yu**

Department of Biomedical Engineering  
College of Future Technology  
Peking University  
sunyu@stu.pku.edu.cn

**Xiang Wenyi**

Electronics  
School of Electrical and Electronic Engineering  
Nanyang Technological University  
WENYI004@e.ntu.edu.sg

## ABSTRACT

Photoacoustic imaging (PAI) suffers from inherent limitations that can degrade the quality of reconstructed results, such as noise, artifacts and incomplete data acquisition caused by sparse sampling or partial array detection. In this study, we proposed a new optimization method for both two-dimensional (2D) and three-dimensional (3D) PAI reconstruction results, called the regularized iteration method with shape prior. The shape prior is a probability matrix derived from the reconstruction results of multiple sets of random partial array signals in a computational imaging system using any reconstruction algorithm, such as Delay-and-Sum (DAS) and Back-Projection (BP). In the probability matrix, high-probability locations indicate high consistency among multiple reconstruction results at those positions, suggesting a high likelihood of representing the true imaging results. In contrast, low-probability locations indicate higher randomness, leaning more towards noise or artifacts. As a shape prior, this probability matrix guides the iteration and regularization of the entire array signal reconstruction results using the original reconstruction algorithm (the same algorithm for processing random partial array signals). The method takes advantage of the property that the similarity of the object to be imitated is higher than that of noise or artifact in the results reconstructed by multiple sets of random partial array signals of the entire imaging system. The probability matrix is taken as a prerequisite for improving the original reconstruction results, and the optimizer is used to further iterate the imaging results to remove noise and artifacts and improve the imaging fidelity. Especially in the case involving sparse view which brings more artifacts, the effect is remarkable. Simulation and real experiments have both demonstrated the superiority of this method.

**Keywords** Iterative regularization method, Shape prior, Probability matrix, Random partial array, Sparse sensor distribution

# 1 Introduction

Photoacoustic imaging (PAI) has emerged as a promising imaging modality that combines the high spatial resolution of ultrasound with the rich optical contrast of biological tissues. [1] This hybrid imaging technique has found wide-ranging applications in biomedical imaging due to its ability to provide detailed structural and functional information, particularly in scenarios such as vascular imaging [2], tumor detection [3], and brain imaging [4]. However, as with many computational imaging systems, PAI suffers from inherent limitations that can degrade the quality of reconstructed results, such as noise, artifacts, and incomplete data acquisition caused by sparse sampling or partial array detection. Traditional image reconstruction methods, while effective to some extent, often struggle to handle such challenges, especially when the imaging system faces conditions like a sparse view or other constraints that exacerbate result artifacts. [5] These approaches may fail to fully exploit the inherent redundancies or structural priors present in the data, leading to suboptimal performance in terms of reconstruction fidelity and artifact suppression.

To tackle these challenges, researchers have utilized iterative reconstruction (IR) methods to enhance result quality when using sparse view. One of the earliest IR approaches for PAI was introduced by Paltauf et al., who iteratively minimized the discrepancies between observed and simulated projections to improve image reconstruction. [6] Subsequent IR techniques incorporated various physical factors related to imaging. Later, Deán-Ben et al. developed a precise model-based 3D reconstruction algorithm that used a sparse matrix model to compute theoretical pressure [7], resulting in fewer artifacts compared to back-projection methods. Wang et al. [8,9] demonstrated that iterative penalized least-squares methods, constructed on discrete-to-discrete imaging models with expansion functions over different fixed spatial grids, and using either quadratic smoothing or total variation (TV) norm constraints, could significantly improve the performance of 3D PAI systems for small animals. Similarly, Huang et al. [10] proposed forward and backward operators based on k-space pseudospectral methodologies. While these IR techniques have shown excellent results, their applicability to large-scale 3D PAI is limited due to the substantial increase in computational and memory demands caused by the scaling of the spatial grid and system matrix. [11] Researchers have, therefore, explored novel alternatives. Arridge et al. addressed this by introducing efficient numerical implementations of adjoint operators for PAI reconstruction and applying compressed sensing via Bregman iteration to reduce sensor requirements. [12] However, their method was computationally expensive and restricted to voxel counts on the scale of  $10^6$ . Shang et al. [13] took a different approach by building a forward model using directly measured graphite point sources, but the inefficiencies in optimization and inaccuracies in the model itself limited its practicality. Deep learning-based methods for PAI reconstruction improve computational efficiency and image quality [14–16] but depend on large, specialized datasets that are hard to obtain and struggle to generalize across different imaging systems or conditions, limiting their clinical applicability.

In this study, we proposed a new optimization method for photoacoustic imaging reconstruction results. The key idea of this method is that the similarity of the imaged object is higher than the noise and artifacts in results of the reconstruction of multiple random partial array signals in the entire imaging array using any reconstruction algorithm, such as DAS and BP, and using these results a probability matrix is obtained through calculation methods. The different positions of the matrix reflect the probability that the position is the real object in the imaging space. As a shape prior [17], this probability matrix guides the iteration and regularization of the entire array signal reconstruction results using the original reconstruction algorithm (the same reconstruction algorithm for processing random partial array signals). This method is not affected by the array distribution, imaging region, etc., and can be used in both 2D and 3D imaging in photoacoustic computational imaging, and can be widely applied to other computational imaging systems, including ultrasound, ct, etc., with strong generalization and robustness. By leveraging the shape prior based on possibility matrix and iteratively refining reconstruction results, this method achieves superior performance compared to the result before the optimization. Both simulation and experimental results demonstrate the effectiveness of the proposed method in reducing noise and artifacts under sparse-view conditions while preserving critical structural information in PAI reconstructions. For the convenience of calling this algorithm, we call it RI-SPPM, RI means that it is a regularized iteration process, SPPM means that the shape prior is based on a probability matrix.

This paper is organized as follows. In Section 2, we present the theoretical framework of the proposed method, detailing the construction of the probability matrix, the integration of the shape prior, and the iterative algorithm employed. Section 3 describes the simulation and experimental results, demonstrating the advantages of our method. Finally, Section 4 concludes the paper by discussing the implications of the proposed method and exploring potential future developments for RI-SPPM in computational imaging applications.

## 2 Method

This part is mainly divided into two parts. The first part is the construction of probability matrix generated by random partial element signals, which provides a shape prior knowledge for subsequent regular iteration; The second part is the specific iteration optimization scheme.

### 2.1 Construction of Probability Matrix

This section begins by introducing the causes of noise and artifacts in photoacoustic imaging, laying the foundation for the rationale of the proposed method. For the construction of the probability matrix, we randomly select a portion of the signal from all array elements for reconstruction. A probability matrix consistent with the dimensions of the reconstruction results is generated using mathematical operations on the obtained reconstruction results. In this matrix, high-probability regions indicate a higher likelihood of representing the true imaged object, while noise and artifacts, due to their randomness, tend to correspond to regions with lower probabilities. Finally, we describe how this shape prior knowledge is utilized in a specific regularized iterative reconstruction process, including the selection of the loss function and the optimizer.

#### 2.1.1 Theoretical Basis: Causes of Noise and Artifacts

**2.1.1.1 Noise** In photoacoustic computational imaging, many kinds of noise may be introduced due to the characteristics of the probe and the working environment, which will affect the image quality. These noises include electronic and thermal noise of the probe itself, frequency distortion due to limited bandwidth, angle-dependent noise due to directivity, mechanical vibration and external acoustic interference, sensitivity or position differences between probe arrays, etc. Among these noises, the electronic thermal noise is generated by electronic components such as resistors in the probe and its signal processing system, and is related to its own temperature. Due to the directivity of the probe, the response to signals from non-optimal angles is weak, resulting in angle-dependent directional noise. The sensitivity error of the array probe is due to the different probe elements in the array may be due to the difference in manufacturing process, resulting in sensitivity and position deviation, resulting in a certain error. Then the noise related to the array elements will appear random with the random selection of the array elements. Therefore, we can take advantage of the fact that the randomness of some noise changes with the array element is higher than that of the imaged object with the array element, so as to remove the noise with high randomness and retain the imaged object with high consistency [18].

**2.1.1.2 Artifacts** Recorded photoacoustic (PA) signals need to undergo a mathematical transformation to form final PA result. The transformation is typically achieved using reconstruction algorithms, such as BP, and IR. However, different reconstruction algorithms possess distinct characteristics and may produce images with different artifacts. Common artifacts in PAI, including negativity artifacts, streak artifacts, splitting artifacts, and reflection artifacts, affect the quality of reconstruction results.

**Streak Artifacts** As the artifact most affected by the probe distribution, Streak artifacts describe undesired structures in an image that have a streak shape. They are a common type of artifacts in PA imaging and are formed due to non-ideal imaging conditions, such as sparse and limited-angle sampling. Most streak artifacts occur around PA absorbers that have stronger optical absorption than their background. The spatial resolution of PA imaging can be greatly impacted by the streak artifacts, especially when strong PA absorbers are present. Figure 1 shows the results of 2D reconstruction under different array configurations. It can be clearly found that this type of artifact is greatly affected by array configurations. Therefore, we can make good use of the characteristic that the randomness of the streak artifact changing with the array is higher than that of the imaged object changing with the array, so as to remove the streak artifact with high randomness and retain the imaging object with high consistency [18].

**Negativity Artifacts** Compared to streak artifacts, negative artifacts are less influenced by the randomness of matrix distribution but are still impacted by its properties. Negativity artifacts refer to unwanted structures in photoacoustic (PA) results that exhibit negative magnitudes. These artifacts are typically found at the edges of PA sources and are considered undesirable because PA results are intended to represent the optical absorbance characteristics of biological tissues, which are inherently positive. Research has indicated that two primary factors contributing to these artifacts are limited detector bandwidth and restricted view angle. When the detector's bandwidth is insufficient, the back-projected (BP) signals become distorted due to the loss of essential frequency components, leading to the emergence of negativity artifacts. Similarly, with a limited view angle, certain PA signals propagating in three-dimensional space may not be captured, resulting in partial data loss and artifact formation. Additionally, a non-ideal acoustic medium can further exacerbate negativity artifacts, as acoustic attenuation, scattering, and refraction may distort the signals. These artifacts are not exclusive to BP algorithms but are also prevalent in other reconstruction approaches, such as time-reversal (TR)

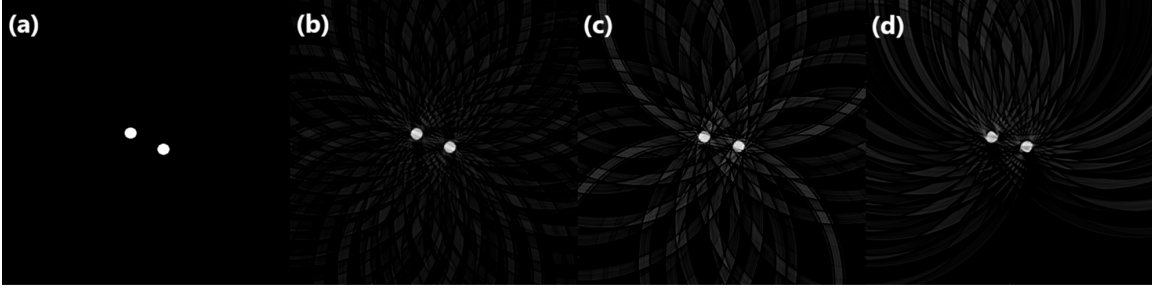


Figure 1: Streak artifacts in PAI. (a) A numerical phantom with two disks. (b) and (c) Reconstructed images using BP with 32 and 16 detectors evenly-distributed on a full ring. (d) Reconstructed images by using half ring (16 detectors)

and frequency-domain methods. As shown in Figure 2, the array distribution has a certain influence on the formation position of negative artifacts. Therefore, we can make good use of the characteristic that the randomness of the negativity artifact changing with the array is higher than that of the imaged object changing with the array, so as to remove the artifact with high randomness and retain the imaging object with high consistency [18].

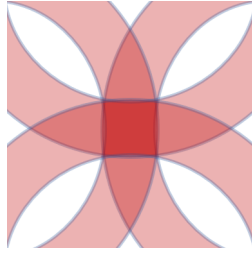


Figure 2: Negativity artifacts schematic diagram (blue is the negative artifact)

**Other Artifacts** For other artifacts, there is no detailed research report or scientific data to show the influence of array properties such as array distribution on artifacts, such as Splitting artifacts, Reflection artifacts, etc., but in general, compared to the real objects to be imitated, Artifacts are intuitively more strongly influenced by element randomness

### 2.1.2 Reconstruction of Random Selected Element Signals

For a computational imaging system with array number  $N$  and sampling number  $M$ , the obtained signal domain data dimension is  $N * M$ . We randomly select  $x$  element signals for reconstruction ( $x < N$ ), here we have  $A$  selections ( $A = C_N^x$ ), and we only need  $A$  random  $k$  results ( $k < A$ ), the  $k$  results are  $R_1, R_2, \dots, R_k$ . (The choices of  $x$  and  $k$  are described in detail in subsequent paragraphs.)

### 2.1.3 Acquisition of Probability Matrix

In three dimensions, the probability matrix is defined as  $P(x, y, z)$ .

$$P(x, y, z) = \int_{v_{\min}}^{v_{\max}} D(x, y, z) \cdot \frac{v - v_{\min}}{v_{\max} - v_{\min}} \cdot \|D(x, y, z) - v > 0\|_0 dv \quad (1)$$

where,

$$v_{\min} = \min(D(x, y, z)), v_{\max} = \max(D(x, y, z))$$

$$D(x, y, z) = \frac{(\frac{1}{k}(R_1 + R_2 + \dots + R_k))^2}{\frac{1}{k}(R_1^2 + R_2^2 + \dots + R_k^2)} = \frac{(R_1 + R_2 + \dots + R_k)^2}{k \times (R_1^2 + R_2^2 + \dots + R_k^2)} \quad (2)$$

In order to have a more intuitive physical meaning for the subsequent regular iteration process, we normalize  $P$  0 – 1. The result after normalization is  $P_N$ .

$$P_N = \frac{P - \min(P)}{\max(P) - \min(P)} \quad (3)$$

The function  $P(x, y, z)$  is introduced as a probabilistic representation of spatial data distributions in three-dimensional space. The function integrates the local property  $D(x, y, z)$ , which quantifies the concentration or

uniformity of measured attributes  $R_1, R_2, \dots, R_k$  at a given point  $(x, y, z)$ , defined as the ratio of the squared arithmetic mean to the mean of squared values. This makes  $D(x, y, z)$  a measure of localized data consistency, where higher values indicate greater uniformity. To account for variations across the defined region,  $P(x, y, z)$  is computed by integrating over the range  $[v_{min}, v_{max}]$ , where these bounds represent the global extremal values of  $D(x, y, z)$ . The integration involves a weighting factor  $\frac{v-v_{min}}{v_{max}-v_{min}} \cdot \|D(x, y, z) - v\|_0$ , which characterizes the probabilistic "importance" of this point within the entire three-dimensional region through weighting and integration range.

## 2.2 Regularized Iteration Optimization

In this section, we will use the probability matrix  $P$  obtained in the previous section as a shape prior and design a suitable loss function for regular iterative optimization of the original reconstruction results of the entire array signal.

### 2.2.1 Shape Prior and Loss Function

**2.2.1.1 Shape Prior** The feasibility of using  $P_N$  as a shape prior lies in the fact that it directly provides the probability distribution information of each voxel or pixel region, which can be used to indicate the model's tendency to strengthen certain regions (high probability regions) in the reconstruction results and its inhibition demand for other regions (low probability regions). This prior information can effectively guide the optimization process, making the result more in line with the expected structural characteristics, while reducing the impact of noise or artifacts. The rational constraint of shape information is realized mathematically, and the optimization stability of shape consistency is improved. It has clear feasibility and physical significance.

**2.2.1.2 Loss Function** The result of reconstructing all array signals using the algorithm to be optimized is  $R_N$ . The result of each iteration optimization is  $R_{op}$ . To enhance the generalizability of the algorithm and reduce the need for extensive parameter adjustments during application,  $R_N$  and  $R_{op}$  are normalized to the range of  $[-1, 1]$  during the data preprocessing stage. The loss function mainly consists of two parts: data consistency item [19] and regularized term [20].

**Data Consistency Item** Loss of data consistency item is represented by  $Loss_{dc}$ .

$$Loss_{dc} = (R_N - R_{op})^2 \quad (4)$$

Its corresponding gradient is  $gradient_{dc}$ .

$$gradient_{dc} = \frac{\partial Loss_{dc}}{\partial R_{op}} = 2 \times (R_N - R_{op}) \quad (5)$$

The role of the data consistency item is to ensure that the optimized results do not deviate too much from the original reconstruction results, thereby maintaining physical consistency and data authenticity with the input data. In the photoacoustic computational reconstruction problem, the result  $R_N$  reconstructed by the initial method to be optimized is obtained by a certain inversion method. Although it may contain noise or error, it is still the basic data closest to the real physical field distribution. Due to the regularization introduced in the optimization process, the  $R_{op}$  of the optimization result may deviate from the original data, and even lose the important features of the original signal. Therefore, the data consistency item can impose constraints in the optimization process, forcing the optimization results to be consistent with the original reconstructed data as much as possible, so that the optimized volume data can gradually de-noise and enhance the structure while still reflecting the main features and information of the input data. This is a balancing mechanism that avoids distortion caused by excessive regularization and strengthens the physical confidence and data integrity of the optimized results.

**Regularized Term** Loss of regularized term is represented by  $gradient_{rg}$ .

$$Loss_{rg} = ((1 - P_N) \times R_{op})^2 \quad (6)$$

Its corresponding gradient is  $gradient_{rg}$ .

$$gradient_{rg} = \frac{\partial Loss_{rg}}{\partial R_{op}} = 2 \times (1 - P_N) \times R_{op} \quad (7)$$

The significance of regularization term is to use the prior knowledge of the problem to constrain the optimization process. As we mentioned in the previous section, in the actual reconstruction, the results obtained by using the traditional reconstruction algorithm are accompanied by noise and artifacts, which makes the reconstruction results rough and even difficult to reflect the real shape of the target. By combining the prior information provided by the prior

probability distribution  $P_N$ , the regularization term can actively suppress the data in the low probability region, thereby reducing the interference of artifacts or noise to the solution in the reconstruction process. The design idea of the regularization term is to guide the optimal solution to cluster in the high probability region (these regions are more in line with the prior physical knowledge), that is, the penalty of the high probability region is low, while the value of the low probability region is suppressed, that is, the penalty of the low probability region is high. This constraint can make the optimization more robust, that is, reduce overly radical updates in areas with greater uncertainty, and ultimately promote the optimized results to have both prior rationality and data authenticity, thus generating reconstruction results with higher reliability.

### 2.2.2 Optimizer Selection and Regularized Iteration Process

**2.2.2.1 Optimizer Selection** We selected the Adam optimizer (Adaptive Moment Estimation) [21] as our optimization algorithm. Adam is a first-order gradient-based optimization algorithm that combines the advantages of Momentum and RMSProp, making the optimization process more stable and efficient in complex reconstruction tasks. Specifically, the momentum mechanism reduces oscillations and gradient noise by applying an exponentially weighted average to the gradients, while RMSProp's adaptive learning rate ensures proper adjustments of the learning rates across different variable dimensions. Additionally, Adam incorporates bias correction, which rectifies the biases during early iterations, thereby improving stability. Overall, with its fast convergence and adaptive features, the Adam optimizer meets the requirements of our task.

**2.2.2.2 Regularized Iteration Process** The following is the specific algorithm pipeline of iterative optimization:

---

#### Algorithm 1

---

```

1: Input:
2:    $R_N$ : Reconstruction results to be optimized  $\triangleright [-1, 1]$ 
3:    $P_N$ : Probability matrix  $\triangleright [0, 1]$ 
4:    $\lambda_{con}, \lambda_{reg}$ : Data consistency term coefficient, regularization coefficient
5:    $lr, num\_iters$ : Learning rate, Number of iterations
6:    $optimizer \leftarrow AdamOptimizer(R_N, lr = learning\_rate)$ 
7: Output:  $R_{op}$ : Iteration result  $\triangleright [-1, 1]$ 
8: for  $iteration \leftarrow 0$  to  $num\_iters$  do
9:   Step 1:
10:     $gradient_{data\_consistency} \leftarrow 2 \times (R_N - R_{op})$ 
11:   Step 2:
12:     $gradient_{prior\_reg} \leftarrow 2 \times (1 - P_N) \times R_{op}$ 
13:   Step 3:
14:     $total\_gradient \leftarrow \lambda_{con} \cdot gradient_{data\_consistency} + \lambda_{reg} \cdot gradient_{prior\_reg}$ 
15:   Step 4:
16:     $new\_lr \leftarrow lr$ 
17:     $optimizer.set\_lr(new\_lr)$ 
18:   Step 5:
19:     $step \leftarrow optimizer.update(total\_gradient)$ 
20:     $R_{op} \leftarrow R_{op} + step$ 
21: end for

```

---

## 3 Result

In this part, we use 3D simulation data and in vivo animal experiment data to verify the performance of RI-SPPM algorithm.

### 3.1 Simulation Data Results

#### 3.1.1 3D PA Image Reconstruction under 1024 Hemispherical System

We first used simulated hand vessels as the target tissue to demonstrate the high performance of the RI-SPPM algorithm. The simulated data is based on the 3D PA imaging results of human peripheral hand vessels from another work [22], which was used as the ground truth. At a grid point spacing of 0.2 mm, the total grid size of the imaging area is 128\*320\*256 (25.6 mm  $\times$  64.0 mm  $\times$  51.2 mm). In order to simulate 3D PA imaging, the radius of the hemispherical

system is 4cm, and a gap with a height of 1cm is opened at the top as the laser light inlet, and the remaining positions are evenly distributed with 1024 array elements(Figure 3 is imaging setup). Then we obtained PA signals collected by these 1024 arrays through forward propagation of the K-Wave toolbox [23].

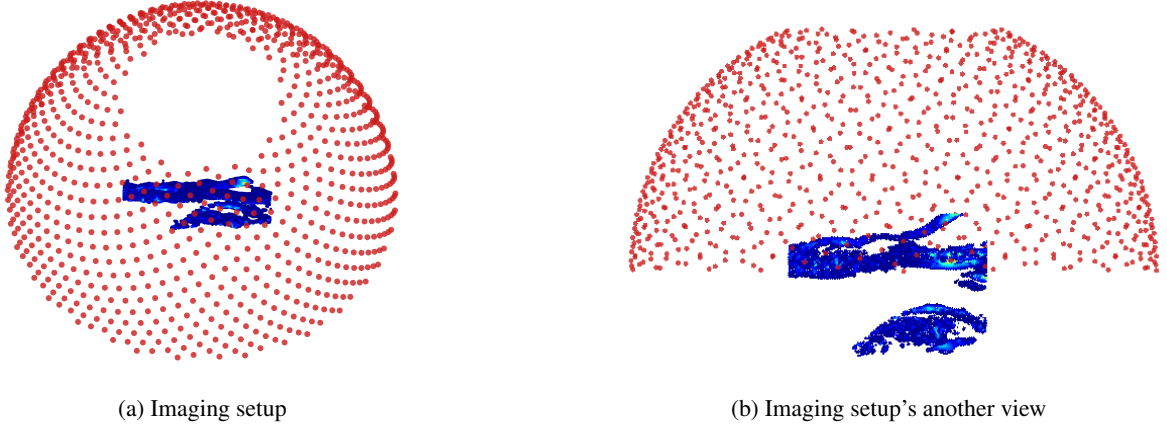


Figure 3: (a) shows the approximate position of the elements and fingers in the system. (b) further shows the position of the fingers and the direction of placement

The above imaging system was selected for simulation to generate sparse photoacoustic signals in order to evaluate the performance of the RI-SPPM algorithm. The simulation is based on 3D photoacoustic imaging data of real hand vasculature as the "ground truth," using a high-resolution grid with a resolution of 0.2 mm ( $128 \times 320 \times 256$ ) to capture the intricate structures of the vasculature. The system is designed as a hemispherical array with a radius of 4 cm, featuring a laser entry point at the top with a height of 1 cm to create a missing-view angle. The array is uniformly distributed with 1024 sensors to simulate a typical photoacoustic imaging device. This simulation approach closely approximates real-world scenarios, provides a controlled evaluation standard, and offers a reliable basis for validating the performance of the RI-SPPM algorithm in photoacoustic imaging.

### 3.1.1.1 Comparison of Results before and after Optimization

In this example, we use the 3D PA result reconstructed by the UBP algorithm as the result optimized by the RI-SPPM algorithm. The distributions of the acoustic source are presented in Figure 4(a), while the reconstruction results are depicted in Figure 4(b-c). For each set of images, the upper and lower subimages correspond to the top-view maximum amplitude projection (MAP) and the front-view MAP of the 3D reconstruction, respectively. In Figure 4(b), the reconstruction results obtained via the UBP algorithm display significant artifacts on the right side of the index finger. These arise because the laser illumination originates from the right side of the index finger, leading to a lack of information from that particular angle and, consequently, severe artifacts. When compared to the ground truth, a substantial discrepancy is evident. As shown in Figure 4(c), the optimization performed by the RI-SPPM algorithm significantly reduces the artifacts in the UBP results, bringing them closer to the ground truth. The artifacts caused by incomplete angular coverage are largely corrected, and additional spurious artifacts in other regions are also mitigated, such as those observed in the middle of the finger's top-view MAP and in the upper and lower areas of the finger's front-view MAP. Furthermore, in the 3D view (Figure 4(e-f)), the improvements in the PA reconstruction results after applying the RI-SPPM algorithm are clearly observable.

Subsequently, we performed a comprehensive mean squared error (MSE) analysis on the reconstruction results before and after optimization (all three datasets are normalized). The MSE between the reconstruction using the UBP algorithm and the ground truth is 0.3398, whereas the MSE after applying the RI-SPPM optimization is reduced to 0.0040. To further demonstrate the effectiveness of the RI-SPPM optimization, and considering that the overall MSE metric may be influenced by the presence of artifacts, we selected a region rich in valid information for detailed analysis and verification. Specifically, we extracted data along two lines. The voxel intensity values along the lines for the three datasets are presented in Figure 5. In Figure 5(b), it is evident that, in regions containing finger information, the intensity curve of the RI-SPPM-optimized result aligns closely with the ground truth, demonstrating superior consistency compared to the UBP-only reconstruction. The correlations before and after using RI-SPPM are 0.65 and 0.92. In Figure 5 (c), it can be seen that in regions lacking finger data, the noise and artifact levels in the RI-SPPM-optimized results are significantly closer to zero, while the noise and artifact levels in the UBP-only reconstruction are considerably higher. The correlations before and after using RI-SPPM are 0.00 and 0.87.

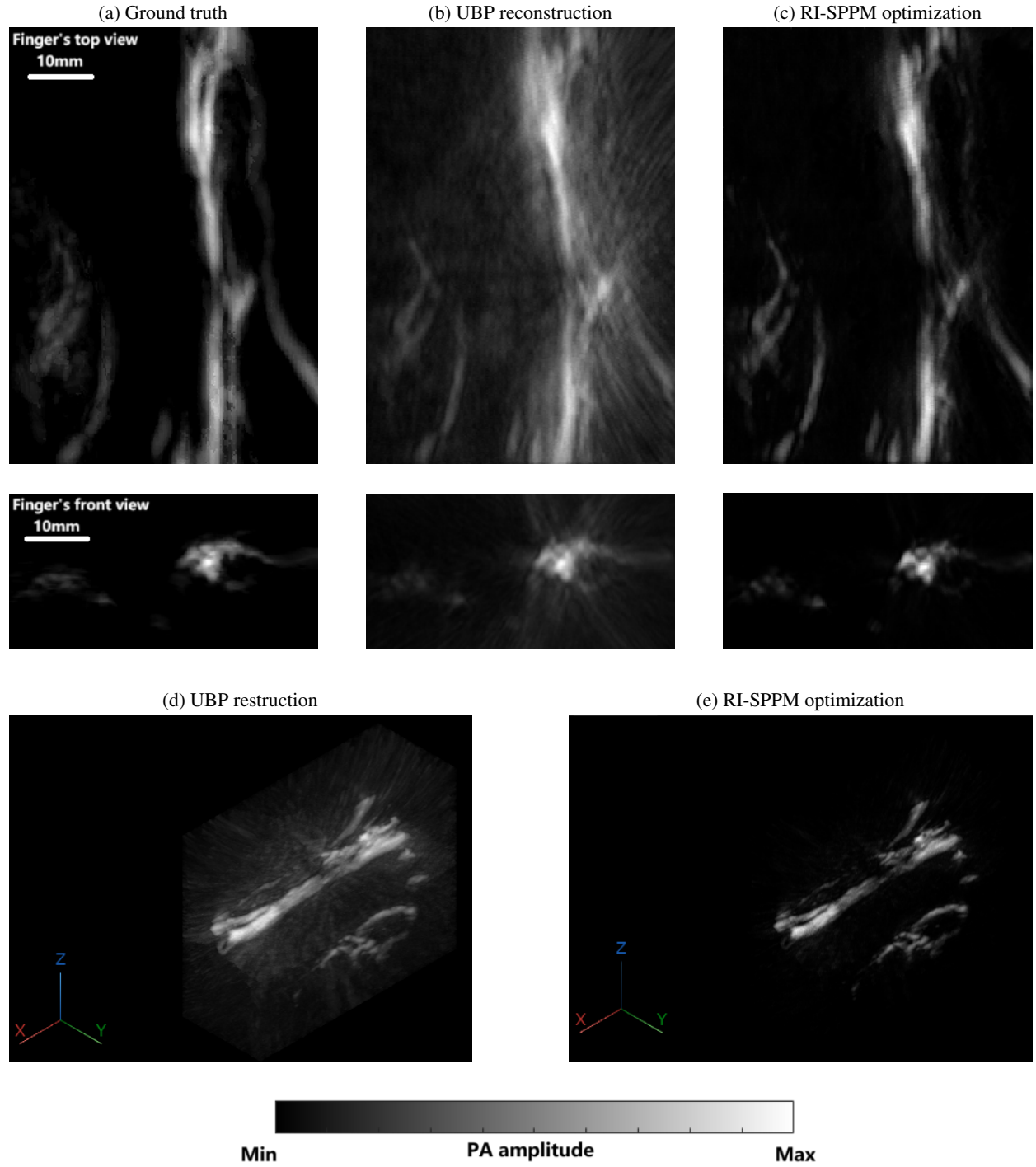


Figure 4: Comparison of 3D photoacoustic reconstruction results under 1024 hemispherical system. (a) Finger's top-view maximum amplitude projection, front-view maximum amplitude projection of the acoustic source. (b) Finger's top-view maximum amplitude projection, front-view maximum amplitude projection of the UBP result. (c) Finger's top-view maximum amplitude projection, front-view maximum amplitude projection of the RI-SPPM result. (d) Reconstruction result of UBP algorithm in 3D-view. (e) Reconstruction result after optimization of RI-SPPM algorithm in 3D-view.



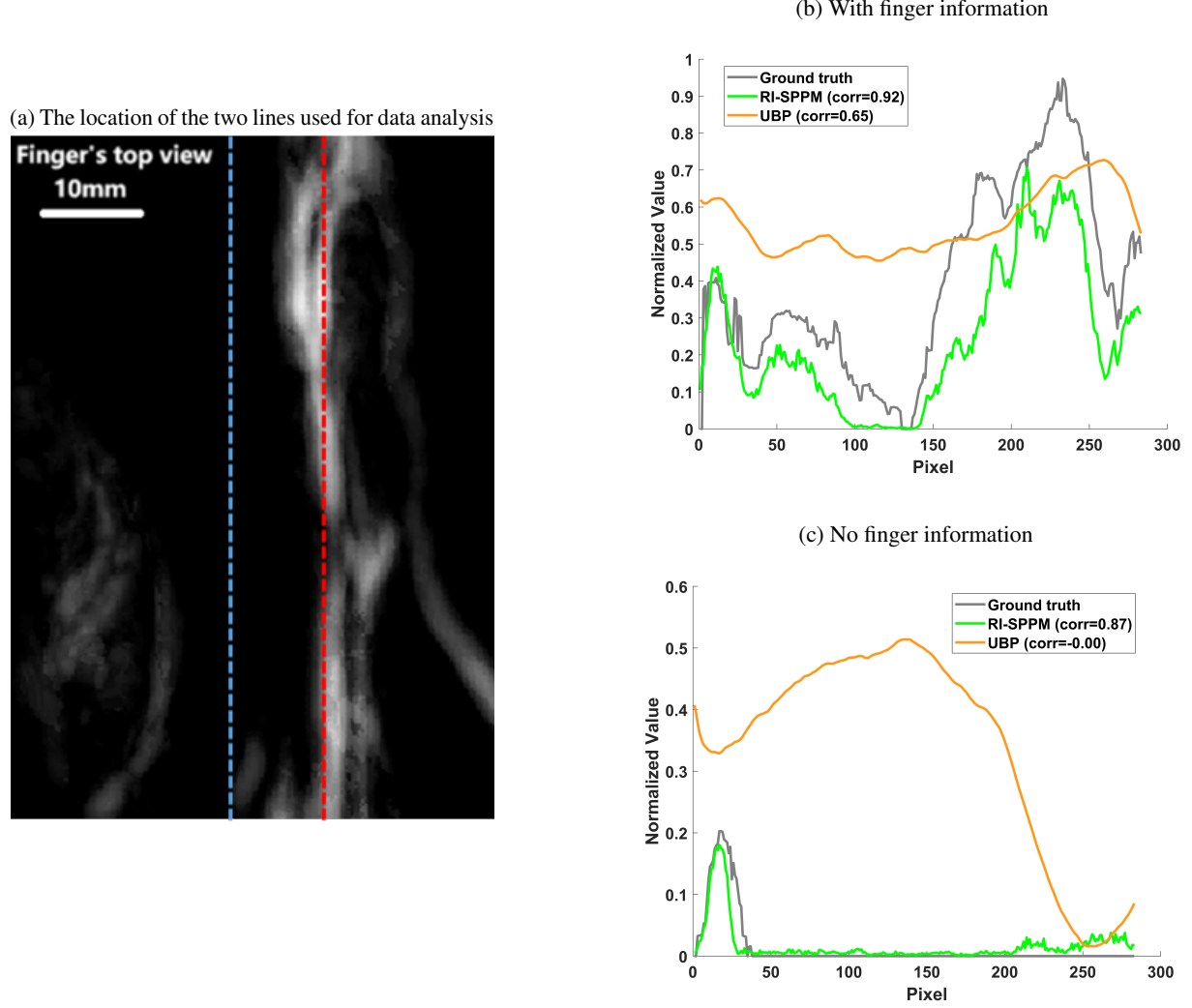


Figure 5: (a) Red line with the finger information and blue line without the finger information. (b) shows the intensity distribution in red line. (c) shows the intensity distribution in blue line.

In conclusion, in the simulation experiments, the reconstruction results obtained using the UBP algorithm and further optimized by the RI-SPPM algorithm demonstrated excellent performance, particularly in artifact suppression, noise reduction, and the preservation and representation of true structural information.

### 3.1.1.2 Parameters Selection and Computing Environment

In this simulation experiment, the specific values of the parameters we used are as follows:

In this experiment, we used a graphics card type GeForce RTX 4090 and the CPU type is AMD® Epyc 9354 32-core processor x 128. In UBP algorithm reconstruction, we use Taichi [24, 25] for GPU acceleration. For the reconstruction with PA signal size of 1024\*4096 and region size of 128\*320\*256, the time consuming is about 0.9s. So the entire RI-SPPM optimization process took less than a minute and 30 seconds. Of course, we have skills in the choice of parameters, and the choice of  $x$  is generally about one-tenth of the total number of elements. We also found that when the initial value of  $l_r$  is about 0.001, the iterative result can be quickly optimized. And the number of iterations is much lower than  $\text{num\_iters}$ .

Parameters	Value
$N$	1024
$M$	4096
$x$	50
$k$	50
$\lambda_{con}$	0.10
$\lambda_{reg}$	0.90
$lr$	0.001
$num\_iters$	500

Table 1: 3D PA image reconstruction under 1024 hemispherical system

### 3.1.2 3D PA Image Reconstruction under 256 Spherical System

We then used a Gaussian sphere and three cylinders as target to demonstrate the high performance of the RI-SPPM algorithm (Figure 6(a)). At a grid point spacing of 0.1 mm, the total grid size of the imaging area is 256\*256\*256 (25.6 mm  $\times$  25.6 mm  $\times$  25.6 mm). In order to simulate 3D PA imaging, the radius of the spherical system is 6cm. Then we obtained PA signals collected by these 256 arrays through forward propagation of the K-Wave toolbox.

#### 3.1.2.1 Comparison of Results before and after Optimization

From a three-dimensional perspective (Figure 6(b,c)), the artifacts significantly decrease after optimization by the RI-SPPM algorithm. The Gaussian sphere and tubular structures are displayed more clearly. Through calculations, the MSE between the UBP reconstructed result and the ground truth is 0.0126, while the MSE of the result optimized by the RI-SPPM algorithm is 0.000146. In conclusion, in the simulation experiments, the reconstruction results obtained using the UBP algorithm and further optimized by the RI-SPPM algorithm demonstrated excellent performance, particularly in artifact suppression, noise reduction, and the preservation and representation of true structural information.

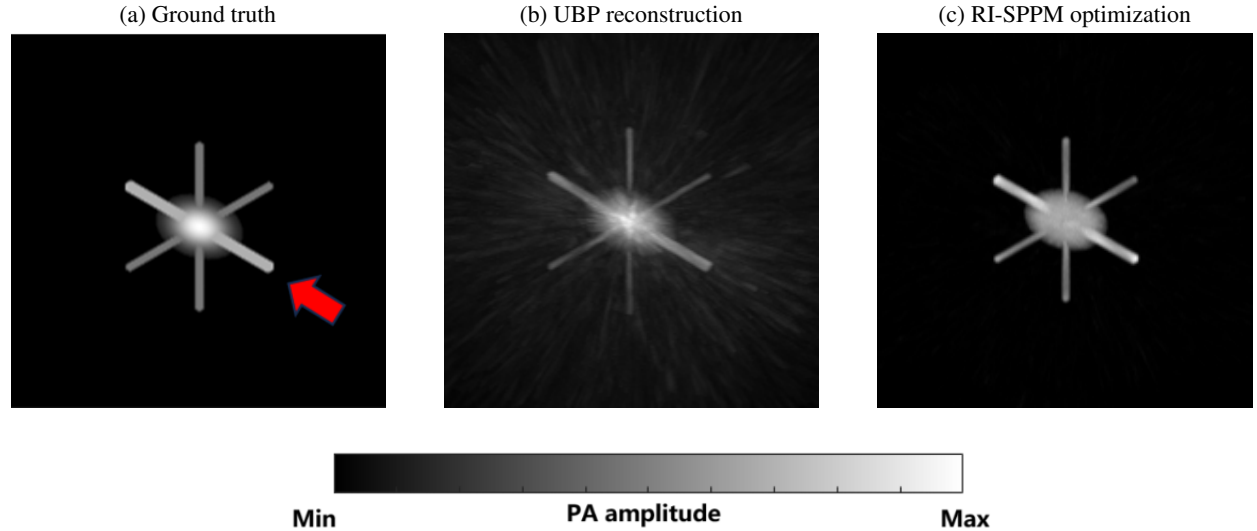


Figure 6: Comparison of 3D photoacoustic reconstruction results under 256 spherical system. (a) Ground truth. (b) Reconstruction result of UBP algorithm in 3D-view. (c) Reconstruction result after optimization of RI-SPPM algorithm in 3D-view.

To better show the contrast, in Figure 7 we use a jet map to display the maximum amplitude projection in the direction of the red arrow in Figure 6(a).

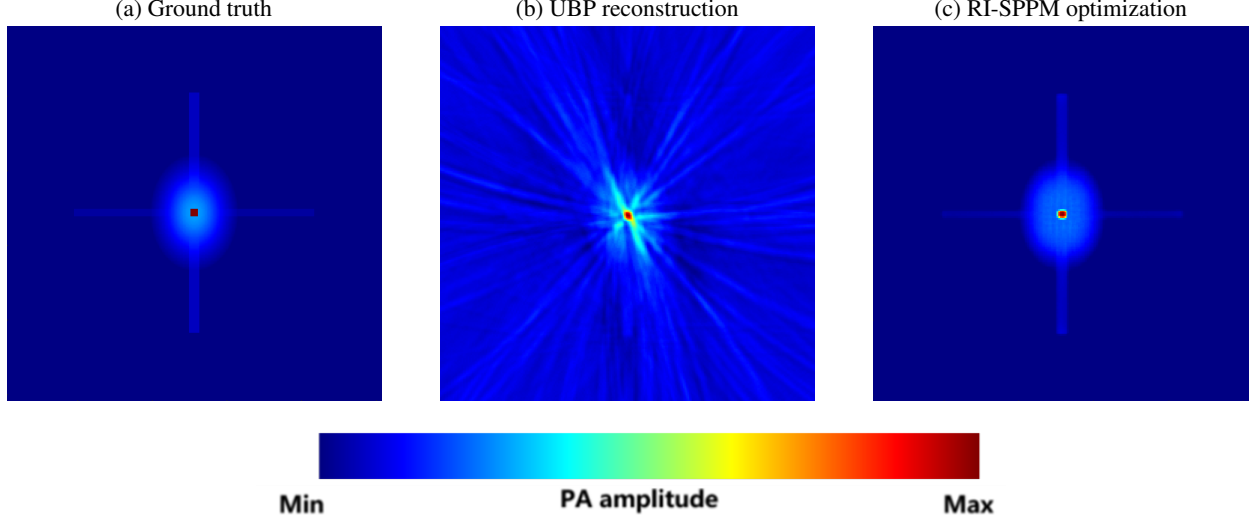


Figure 7: Comparison of 3D photoacoustic reconstruction results under 256 spherical system. (a) The maximum amplitude projection of ground truth. (b) The maximum amplitude projection of the UBP result. (c) The maximum amplitude projection of the RI-SPPM result.

### 3.1.2.2 Parameters Selection and Computing Environment

In this simulation experiment, the specific values of the parameters we used are as follows:

Parameters	Value
$N$	256
$M$	4096
$x$	25
$k$	50
$\lambda_{con}$	0.10
$\lambda_{reg}$	0.90
$lr$	0.001
$num\_iters$	500

Table 2: 3D PA image reconstruction under 256 spherical system

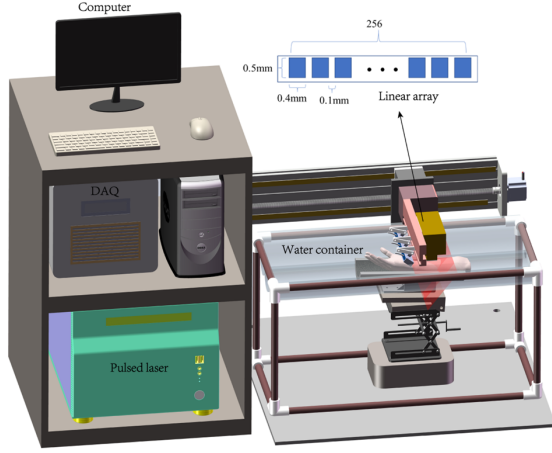
In this experiment, we used a graphics card type GeForce RTX 4090 and the CPU type is AMD® Epyc 9354 32-core processor x 128. In UBP algorithm reconstruction, we use Taichi for GPU acceleration. For the reconstruction with PA signal size of 256\*4096 and region size of 256\*256\*256, the time consuming is about 0.8s. So, the entire RI-SPPM optimization process took less than a minute and 30 seconds. Of course, we have skills in the choice of parameters, and the choice of  $x$  is generally about one-tenth of the total number of elements. We also found that when the initial value of  $lr$  is about 0.001, the iterative result can be quickly optimized. The number of iterations is much lower than  $num\_iters$ .

## 3.2 In Vivo Human Experiment Results

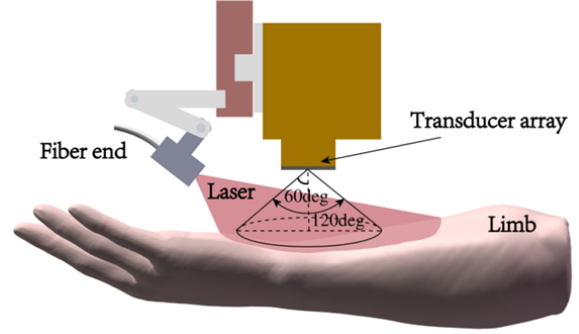
### 3.2.1 3D PA image reconstruction under synthetic matrix array

Then in vivo human study data, including human arm was acquired by Shuang Li’s work [22] using synthetic matrix array. The system employed a nonfocusing linear array (customized by Imasonics, France) to receive PA signals. The linear array has 256 elements with a pitch of 0.5 mm and a kerf of 0.1 mm, i.e., a total length of 12.8 cm. The center frequency of the ultrasonic array is 3.5 MHz with over 80% bandwidth. PA signal is amplified 1500 times via self-built two-stage amplifier, and then received by a data acquisition system (Marsonics DAQ, Tianjin Langyuan Technology

Co., Ltd. China) at 40 MHz sampling rate. The system is shown in Figure 7.



(a) 3D PA imaging system



(b) Schematic diagram of fiber optic illumination and one-dimensional array

Figure 8: (a) shows the 3D PA imaging system. (b) shows details of the core of the system [22]

In the original work, a linear array consisting of 256 elements was moved 2969 times, with a step size of 0.1 mm for each movement, resulting in a large-scale synthetic matrix of  $256 \times 2969$  elements. To create a sparse-view setup for better evaluation of the RI-SPPM algorithm's performance, we extracted 120 rows at equal intervals (approximately 25% of the original data), which corresponds to a step size of 2.5 mm for each scan of the linear array.

### 3.2.2 Comparison of Results before and after Optimization

In this experiment, we utilized the RI-SPPM algorithm to optimize the reconstruction results obtained from the UBP algorithm. The detailed comparison of results before and after optimization is presented in Figure 8.

We compared the hand imaging results before and after the RI-SPPM optimization of the UBP reconstruction. From the top-view perspective, the optimization significantly reduced noise, and both thick and thin blood vessels were displayed more clearly. From the front-view perspective, in addition to making the vascular information more distinct, the lateral noise at the bottom was also effectively suppressed. These findings demonstrate that the reconstruction quality after RI-SPPM optimization is exceptionally high.

In conclusion, in vivo human experiment, the reconstruction results obtained using the UBP algorithm and further optimized by the RI-SPPM algorithm also demonstrated excellent performance, particularly in artifact suppression, noise reduction, and the preservation and representation of true structural information.

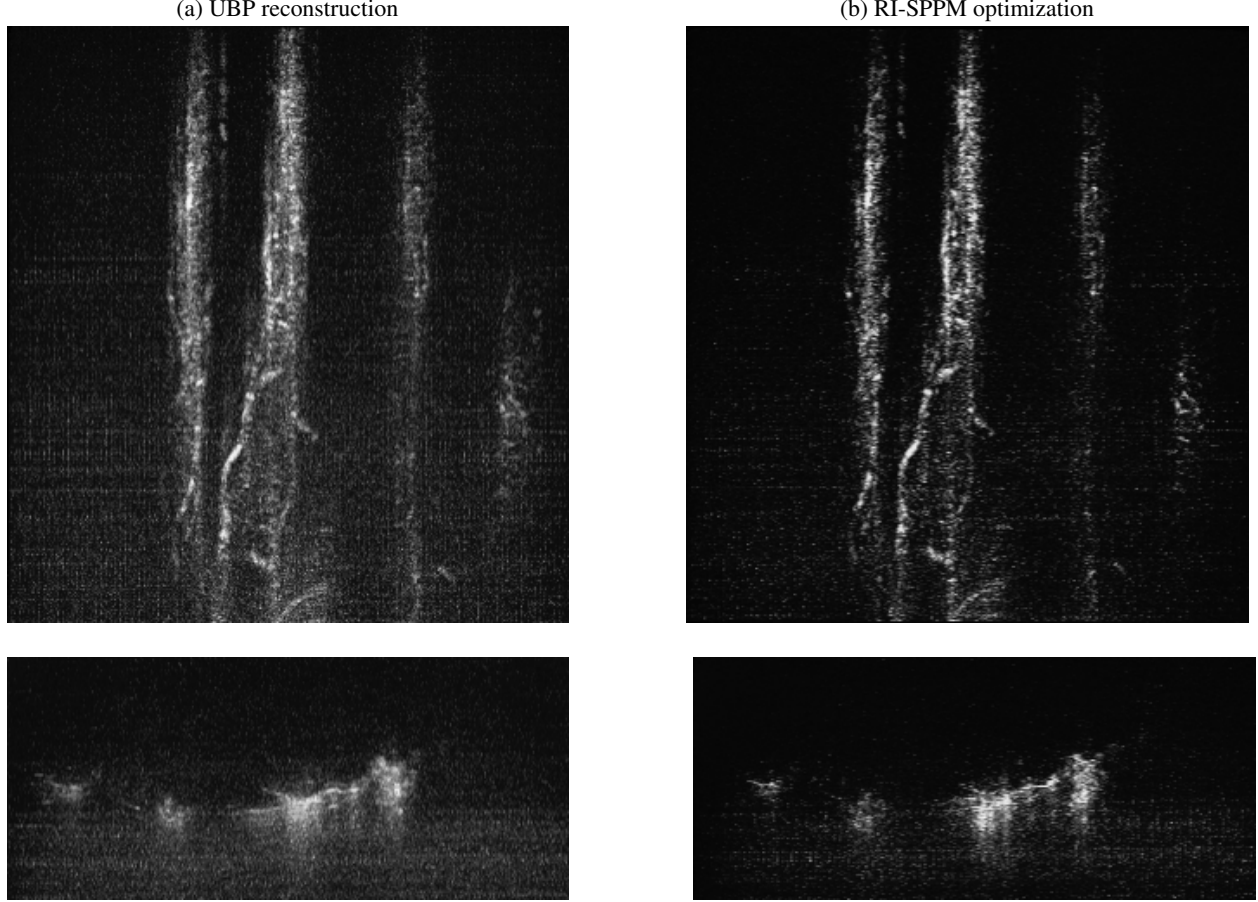


Figure 9: Comparison of 3D photoacoustic reconstruction results under synthetic matrix array. (a) Hand’s top-view maximum amplitude projection, front-view maximum amplitude projection of the UBP results. (b) Hand’s top-view maximum amplitude projection, front-view maximum amplitude projection of the RI-SPPM results.

### 3.2.3 Parameters Selection and Computing Environment

In this animal experiment, the specific values of the parameters we used are as follows:

Parameters	Value
$N$	30720
$M$	2048
$x$	4000
$k$	50
$\lambda_{con}$	0.10
$\lambda_{reg}$	0.90
$lr$	0.001
$num\_iters$	500

Table 3: 3D PA image reconstruction under synthetic matrix array

In this experiment, we used a graphics card type GeForce RTX 4090 and the CPU type is AMD® Epyc 9354 32-core processor x 128. In UBP algorithm reconstruction, we use Taichi for GPU acceleration. For the reconstruction

with PA signal size of  $30720 \times 2048$  and region size of  $625 \times 600 \times 250$ , the time consuming is about 10.2s. For the reconstruction with PA signal size of  $4000 \times 2048$  and region size of  $625 \times 600 \times 250$ , the time consuming is about 3.5s. So the entire RI-SPPM optimization process took less than 7 minutes.

## 4 Discussion and Future

In this study, we focus on demonstrating the optimization effectiveness of the RI-SPPM algorithm applied to the reconstruction results of the UBP algorithm in the context of 3D imaging systems. Through a series of specific experiments, the RI-SPPM algorithm has shown exceptional performance in both simulated studies and live small animal experiments. Notably, from a theoretical perspective, the RI-SPPM algorithm is not constrained to a specific imaging dimension, making it applicable to both 3D and 2D imaging scenarios. Moreover, the core concept of the RI-SPPM algorithm lies in optimizing existing imaging results rather than directly reconstructing images within the signal domain. This unique characteristic grants the algorithm broad applicability, enabling effective suppression of noise and artifacts caused by transducer-related factors (e.g., transducer distribution and other system properties). Importantly, the RI-SPPM optimization is not tied to a specific reconstruction algorithm; other algorithms can also benefit from its enhancement capabilities.

Furthermore, the potential applications of the RI-SPPM algorithm extend beyond photoacoustic computed tomography. Theoretical analysis suggests that the algorithm could be generalized to other imaging fields, such as ultrasound imaging, computed tomography (CT), and various other medical imaging or industrial inspection scenarios. In these fields, the sampling and imaging processes of various devices may also introduce artifacts and noise that vary with the properties of the transducers. In such cases, the RI-SPPM algorithm is expected to offer significant assistance.

Going forward, we plan to expand our research in two key directions. Firstly, we aim to further investigate the optimization capabilities of the RI-SPPM algorithm across a broader spectrum of existing reconstruction algorithms, exploring its adaptability under diverse imaging conditions, modalities, and algorithmic outputs. Secondly, we intend to extend the application of the RI-SPPM algorithm to other areas, such as ultrasound imaging, CT, and potentially other advanced medical imaging techniques like magnetic resonance imaging (MRI) and positron emission tomography (PET). These efforts would further validate its extensive practical value and generalizability.

In the long term, we aspire to make the RI-SPPM algorithm an essential tool for a wide range of imaging systems. Through continued optimization and extension studies, this algorithm has the potential to provide comprehensive solutions for improving imaging quality, resolution, and reliability across diverse application scenarios.

## References

- [1] Li C and Wang L.V. Photoacoustic tomography and sensing in biomedicine. *Phys Med Biol*, 54(19):R59–R97, 2009. doi: 10.1088/0031-9155/54/19/R01. PMID: 19724102; PMCID: PMC2872141.
- [2] C. G. A. Hoelen, F. F. M. de Mul, R. Pongers, and A. Dekker. Three-dimensional photoacoustic imaging of blood vessels in tissue. *Opt. Lett.*, 23:648–650, 1998.
- [3] Jan G. Laufer, Edward Z. Zhang, Bradley E. Treeby, Benjamin T. Cox, Paul C. Beard, Peter Johnson, and Barbara Pedley. *In vivo* preclinical photoacoustic imaging of tumor vasculature development and therapy. *J. Biomed. Opt.*, 17(5):056016, 2012. doi: <https://doi.org/10.1117/1.JBO.17.5.056016>.
- [4] Junjie Yao and Lihong V. Wang. Photoacoustic brain imaging: from microscopic to macroscopic scales. *Neurophoton.*, 1(1):011003, 2014. doi: <https://doi.org/10.1117/1.NPh.1.1.011003>.
- [5] Chao Tian, Kang Shen, Wende Dong, Fei Gao, Kun Wang, Jiao Li, Songde Liu, Ting Feng, Chengbo Liu, Changhui Li, Meng Yang, Sheng Wang, and Jie Tian. Image reconstruction from photoacoustic projections. *Photon. Insights*, 3(3):R06, 2024. doi: <https://doi.org/10.3788/PI.2024.R06>.
- [6] Paltauf, G., Viator, J., Prah, S., and Jacques, S. Iterative reconstruction algorithm for optoacoustic imaging. *The Journal of the Acoustical Society of America*, 112(4):1536–1544, 2002.
- [7] Deán-Ben, X.L., Buehler, A., Ntziachristos, V., and Razansky, D. Accurate model-based reconstruction algorithm for three-dimensional optoacoustic tomography. *IEEE Transactions on Medical Imaging*, 31(10):1922–1928, 2012.
- [8] Wang, K., Su, R., Oraevsky, A.A., and Anastasio, M.A. Investigation of iterative image reconstruction in three-dimensional optoacoustic tomography. *Physics in Medicine & Biology*, 57(17):5399, 2012.
- [9] Wang, K., Schoonover, R.W., Su, R., Oraevsky, A., and Anastasio, M.A. Discrete imaging models for three-dimensional optoacoustic tomography using radially symmetric expansion functions. *IEEE Transactions on Medical Imaging*, 33(5):1180–1193, 2014.
- [10] Huang, C., Wang, K., Nie, L., Wang, L.V., and Anastasio, M.A. Full-wave iterative image reconstruction in photoacoustic tomography with acoustically inhomogeneous media. *IEEE Transactions on Medical Imaging*, 32(6):1097–1110, 2013.
- [11] Zhu, J., Huynh, N., Ogunlade, O., Ansari, R., Lucka, F., Cox, B., and Beard, P. Mitigating the limited view problem in photoacoustic tomography for a planar detection geometry by regularized iterative reconstruction. *IEEE Transactions on Medical Imaging*, 42(9):2603–2615, 2023.
- [12] Arridge, S.R., Betcke, M.M., Cox, B.T., Lucka, F., and Treeby, B.E. On the adjoint operator in photoacoustic tomography. *Inverse Problems*, 32(11):115012, 2016.
- [13] Shang, R., Archibald, R., Gelb, A., and Luke, G.P. Sparsity-based photoacoustic image reconstruction with a linear array transducer and direct measurement of the forward model. *Journal of Biomedical Optics*, 24(3):031015, 2019.
- [14] Hauptmann, A., Lucka, F., Betcke, M., Huynh, N., Adler, J., Cox, B., Beard, P., Ourselin, S., and Arridge, S. Model-based learning for accelerated, limited-view 3-d photoacoustic tomography. *IEEE Transactions on Medical Imaging*, 37(6):1382–1393, 2018.
- [15] Hauptmann, A., and Cox, B. Deep learning in photoacoustic tomography: current approaches and future directions. *Journal of Biomedical Optics*, 25(11):112903, 2020.
- [16] Zheng, W., Zhang, H., Huang, C., Shijo, V., Xu, C., Xu, W., and Xia, J. Deep learning enhanced volumetric photoacoustic imaging of vasculature in human. *Advanced Science*, 10(29):2301277, 2023.
- [17] Chen, Y., Tagare, H.D., Thiruvenkadam, S., *et al.* Using Prior Shapes in Geometric Active Contours in a Variational Framework. *International Journal of Computer Vision*, 50:315–328, 2002. doi: <https://doi.org/10.1023/A:1020878408985>.
- [18] Tian C, Zhang C, Zhang H, Xie D, and Jin Y. Spatial resolution in photoacoustic computed tomography. *Rep Prog Phys*, 84(3), 2021. doi: 10.1088/1361-6633/abdab9. PMID: 33434890.
- [19] M. Lustig, D. L. Donoho, J. M. Santos, and J. M. Pauly. Compressed Sensing MRI. *IEEE Signal Processing Magazine*, 25(2):72–82, March 2008. doi: 10.1109/MSP.2007.914728.
- [20] E. J. Candes, J. Romberg, and T. Tao. Robust uncertainty principles: exact signal reconstruction from highly incomplete frequency information. *IEEE Transactions on Information Theory*, 52(2):489–509, Feb. 2006. doi: 10.1109/TIT.2005.862083.

- [21] Diederik P. Kingma and Jimmy Ba. Adam: A Method for Stochastic Optimization. *CoRR*, abs/1412.6980, 2014. URL: <https://api.semanticscholar.org/CorpusID:6628106>.
- [22] Shuang Li, Guangjie Zhang, Yibing Wang, Wenzhao Li, Yu Sun, and Changhui Li. Photoacoustic imaging of peripheral vessels in extremities by large-scale synthetic matrix array. *Journal of Biomedical Optics*, 29(S1):S11519–S11519, 2024. Publisher: Society of Photo-Optical Instrumentation Engineers.
- [23] Bradley E. Treeby and Benjamin T. Cox. k-Wave: MATLAB toolbox for the simulation and reconstruction of photoacoustic wave fields. *J. Biomed. Opt.*, 15(2):021314, 2010. doi: <https://doi.org/10.1117/1.3360308>.
- [24] Yuanming Hu, Tzu-Mao Li, Luke Anderson, Jonathan Ragan-Kelley, and Frédo Durand. Taichi: a language for high-performance computation on spatially sparse data structures. *ACM Transactions on Graphics (TOG)*, 38(6), December 2019. doi: 10.1145/3355089.3356506. URL: <https://doi.org/10.1145/3355089.3356506>.
- [25] Yibing Wang and Changhui Li. Comprehensive framework of GPU-accelerated image reconstruction for photoacoustic computed tomography. *Journal of Biomedical Optics*, 29(6), June 2024. doi: 10.1117/1.JBO.29.6.066006. URL: <https://doi.org/10.1117/1.JBO.29.6.066006>.